

Exploiting the Final Component of Generator Architectures for AI-Generated Image Detection

Yanzhu Liu

Institute for Infocomm Research,
A*STAR, Singapore

liu_yanzhu@a-star.edu.sg

Yuexuan Wang

Institute for Infocomm Research,
A*STAR, Singapore

wang_yuexuan@a-star.edu.sg

Xiao Liu

Institute for Infocomm Research,
A*STAR, Singapore

liu_xiao@a-star.edu.sg

Mondal Soumik

Institute for Infocomm Research,
A*STAR, Singapore

soumik_mondal@a-star.edu.sg

Abstract

With the rapid proliferation of powerful image generators, accurate detection of AI-generated images has become essential for maintaining a trustworthy online environment. However, existing deepfake detectors often generalize poorly to images produced by unseen generators. Notably, despite being trained under vastly different paradigms, such as diffusion or autoregressive modeling, many modern image generators share common final architectural components that serve as the last stage for converting intermediate representations into images. Motivated by this insight, we propose to “contaminate” real images using the generator’s final component and train a detector to distinguish them from the original real images. We further introduce a taxonomy based on generators’ final components and categorize 21 widely used generators accordingly, enabling a comprehensive investigation of our method’s generalization capability. Using only 100 samples from each of three representative categories, our detector—fine-tuned on the DI-NOv3 backbone—achieves an average accuracy of 98.83% across 22 testing sets from unseen generators.

1. Introduction

“Last in Line, yet First to Reveal.”

— Inspired by Sherlock Holmes

When examining objects like a careful detective, the last touch often reveals the most, having overwritten the layers of history beneath it. Likewise, when determining whether an image is real or AI-generated, the key is to examine the distinctive traces left by the generator, particularly those

from its final stage. Contemporary image generators are no longer monolithic; rather, they comprise multiple modular components operating in stages. This raises a natural and important question: does the last component, which serves as the final step in producing the image, leave identifiable evidence that can be exploited for detection? Our intuition is that, regardless of the generation paradigm—generative adversarial [16], diffusion-based [19], autoregressive [34], or otherwise—there inevitably exists a concluding step that transforms intermediate representations into pixels, serving as the generator’s “final touch”.

We approach this question from the perspective of generation architecture. To clarify, the **architecture** refers to the structural design of a network, including its functional components and their interconnections. A network **component** is a functional module composed of multiple neural layers, such as a VAE decoder, DiT transformer, or tokenizer. In contrast, the generation **model** denotes a specific instantiation of trained weights (e.g., a pretrained network and its fine-tuned variant are considered different models). Most existing deepfake detection methods operate at the model level. They typically generate training samples from particular generation models and design sophisticated features—such as CLIP embeddings [51], frequency-domain cues [35], multi-scale representations [25], reverse-engineered traces [22], or gradient-based signals [14]—to distinguish synthetic images from real ones. However, as new generators continue to emerge, the generalizability of these methods becomes a critical concern. When the distribution of testing data shifts significantly, these approaches often require regenerating of synthetic images from new generation models to retrain the detectors. This challenge is further amplified when users fine-tune generation models

on custom data and keep the resulting models private.

Since real images are readily available from public datasets for image-related tasks (e.g., ImageNet [13], MSCOCO [28]), we propose to “contaminate” real images with generation traces using only the generator’s final component, and subsequently train a detector to differentiate them from the original real images. Operating samples through a single component is substantially faster than executing the entire generation pipeline, particularly in diffusion models that require iterative multi-step inference. Moreover, this strategy does not necessitate the generator to be open-sourced; gray-box access to its final component suffices for implementation.

The potential generalizability of the proposed approach is motivated by three key observations: (a) many generators share similar or even identical final components; (b) relying on only a small fraction of the total parameters reduces overfitting to specific generators; (c) the contaminated images preserve identical semantic content to their real counterparts, ensuring that the detector focuses on generation artifacts rather than semantic information.

To comprehensively validate our hypothesis regarding the generalizability of the generator’s final component, we propose a novel taxonomy that categorizes image generators according to their final architectural component and analyze 21 widely used generators under this framework. Traditionally, image generators are grouped by generation paradigm into three major categories [47]: Generative Adversarial Networks, Diffusion Models, and more recently, Autoregressive Models. However, many recent generators frequently reuse common components based on their function, such as the VAE decoder, which decodes images from latent space.

From our taxonomy, we identify three representative final components—VAE decoder, super-resolution diffuser, and VQ de-tokenizer—and employ them to imprint traces onto real images as part of our approach. We conduct a series of experiments on them to investigate: whether the final component alone is sufficient to detect images generated by its corresponding full architecture; whether a detector trained on one component generalizes to images generated by architectures from other categories; and whether the detector remains effective on fine-tuned variants of the same component. Finally, we select 100 samples from each of the three components using K-medoids clustering, combining the 300 samples to fine-tune a detector built upon a pretrained DINOv3 [39] backbone with an appended fully-connected layer. The resulting detector achieves strong zero-shot performance across multiple challenging benchmarks.

The contributions of this study are as follows:

- We propose examining the final component of image generation architectures as a source of identifiable traces, en-

abling the generalizable detection.

- We introduce a novel taxonomy of text-to-image generators based on their final architectural component, which provides insight into generalization between generators.
- By imprinting traces onto real images and training a fine-grained, region-based detector on them, our model achieves state-of-the-art zero-shot performance across generator categories and challenging benchmarks.

2. Related Work

2.1. Architecture attribution

For the deepfake detection task that this study focuses on, exploration from the perspective of generative architectures remains limited. While for the related task of synthesized image attribution, which aims to identify the generator responsible for a given image, few studies have investigated attribution at the architectural level. Yang et al. [50] claimed to be the first to explore architecture attribution. They assessed GAN architectures and found that architectures leave globally consistent fingerprints, whereas models produce regional traces. Wißmann et al. [48] and Xu et al. [49] reveal that similar diffusion architectures produce similar patterns in frequency-domain features. Furthermore, Abady et al. [1] proposed a Siamese network to verify whether two images originate from the same generation architecture, while Shahid et al. [38] applied one-class classification for open-set architecture scenarios.

2.2. Last step inversion

Few studies have examined the final step of the generation process. Laszkiewicz et al. [23] extracted features of generated images by approximating the inputs just before the final layer. The last step they focused on is a single-layer, e.g., activations, fully connected layer, or attention heads. In contrast, our study targets middle grained functional components. [46] proposed a reverse-engineering approach to map the images back to latent features. To effectively invert the decoder, they used the output from the corresponding encoder as the initialization. While related to our sample construction method for the VAE category, their work focused on model attribution and was limited to latent-based generators.

2.3. Zero-shot deepfake detection

In the zero-shot setting, the detection model is trained on samples from certain generators and applied directly to test images without fine-tuning or any prior knowledge of the generating models. Existing zero-shot methods can be broadly grouped into three categories. **Signal-level fingerprint construction** extracting low-level artifacts as detection cues, such as image gradients (LGrad [14]), pixel neighborhood differences (NPR [24]), or generator noise

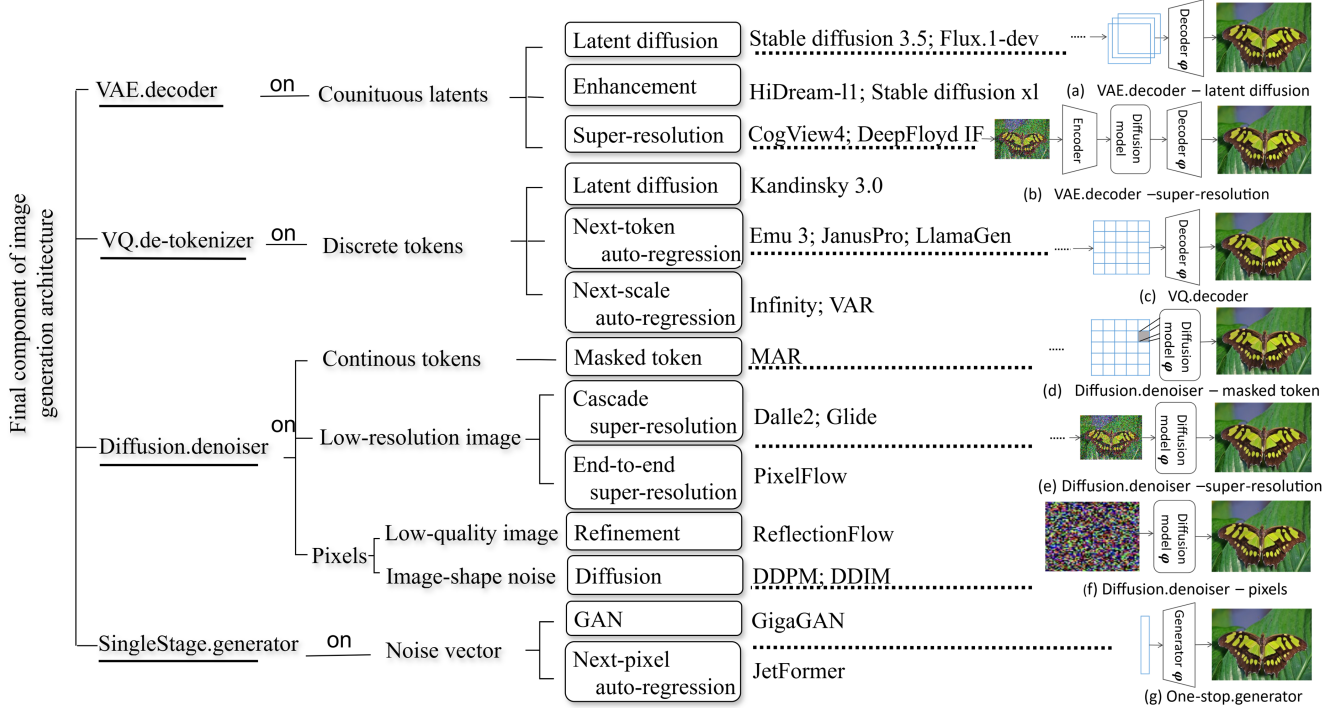


Figure 1. The proposed taxonomy of generation architectures based on final component.

patterns (DIRE [22]); **CLIP-based approaches** relying solely on CLIP image features extracted from different transformer layers (UnivFD [53], RINE [30]), or incorporating text guidance using captions or prompts (e.g., “real” vs. “AI-generated”) to steer classification (DeFake [32], C2P-CLIP [51], LATEST [8]); **Robust feature design** building more resilient features, such as fusing frequency-space features (AIDE [35]) or learning multi-scale features through contrastive learning (CoDE [25]). However, none of these methods explicitly account for the influence of the generator’s architecture or components on the generated images—a gap our approach aims to address.

3. A Taxonomy of Generation Architectures based on Final Component

To facilitate the exploration of common final components in modern generation architectures and the generalizable traces they leave behind, we propose a novel taxonomy that categorizes image generators according to their final architectural component. Let $\varphi(\mathbf{z}) : \mathbb{S}^d \rightarrow \mathbb{R}^{h \times w \times 3}$ denote this final component, where \mathbb{S}^d represents the internal latent space. The design principles of our taxonomy, grounded in $\varphi(\mathbf{z})$, are as follows:

- **Position—Last:** The output of $\varphi(\mathbf{z})$ must be an image in RGB space $\mathbb{R}^{h \times w \times 3}$. We define the taxonomy categories based on the input \mathbf{z} and its input space \mathbb{S}^d .
- **Granularity—Middle-level:** Deep network units can be

considered at four levels of granularity. The finest level refers to individual layers, such as activation or pooling layers. The second level refers to blocks composed of multiple layers that serve highly detailed functions, such as upsampler in U-Net or transformer heads. The coarsest level is the entire model. “Component” lies in the third level, representing a functional module that operates independently, such as VAE decoders or VQ de-tokenizer. This choice is motivated by two factors: many generators release pre-trained weights for such components separately, making them more accessible without the full pipeline; and fine-grained units, like individual layers or small blocks, leave traces that are too subtle or indistinct for reliable detection.

- **Perspective—Implementation.** The taxonomy is based on functional implementation rather than the high-level role of the component. For example, as MAR [26] performs autoregressive prediction over masked tokens but ends with a diffusion denoiser, it is categorized as “denoiser” rather than “de-tokenizer” like other autoregressive generators. DeepFloyd IF [12] performs super-resolution in latent space and ends with a VAE decoder, placing it in the decoder category rather than denoiser like other super-resolution generators.

As illustrated in Fig.1, we define four primary categories based on the input space \mathbb{S}^d , and further subdivide them according to what \mathbf{z} represents, as discussed in Sections

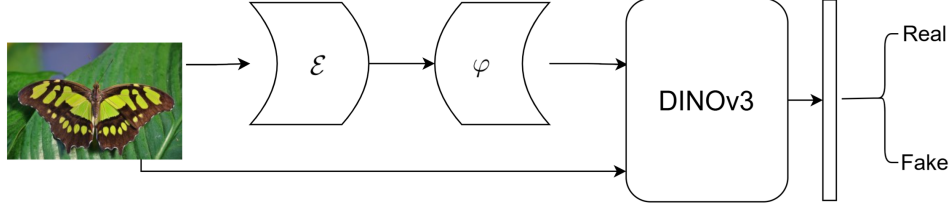


Figure 2. The proposed framework for detecting AI-generated images

3.1-3.4. The categorization of all representative generators in our proposed taxonomy is based on their official source code or released documentation, with detailed references provided in the Appendix.

3.1. VAE.decoder

In the category of VAE.decoder, the final component $\phi(\mathbf{z})$ operates in a continuous latent space, i.e., $\mathbb{S}^d := \mathbb{R}^d$, where $d \ll h \times w \times 3$. It decodes a d -dimensional feature map or vector into the final image. As many modern generators target high-resolution outputs (e.g., 2048×2048), they often perform generation in a low-dimensional latent space for computational efficiency, relying on encoder–decoder structures for dimensionality reduction and expansion.

There are three typical functional contexts in which \mathbf{z} resides: (1) **Latent diffusion**, where diffusion models operate directly in the latent space, as in the Stable Diffusion family [41] and FLUX [7]. As illustrated in Fig.1(a), in this case, \mathbf{z} represents the denoised latent sample predicted by the diffusion model. (2) **Enhancement**, where the latent representation from the diffusion model is further refined—e.g., via GAN-based distillation—to produce a more precise \mathbf{z} before decoding, as in HiDream [5]. (3) **Latent super-resolution**, where a low-resolution image is first generated and then progressively upsampled through latent-space super-resolution stages. As shown in Fig.1(b), the low-resolution image is noised, resized to the target size, and encoded into a latent space for diffusion processing. The resulting upsampled latent, \mathbf{z} , is then decoded to produce the final high-resolution image. Examples include CogView 4 [52] and DeepFloyd IF [12], which employ the Stable Diffusion 4xUpscaler [37] as the final super-resolution stage.

3.2. VQ.de-tokenizer

The final component of VQ.detokenizer generators operates in discrete token space, i.e., $\mathbb{S}^d := \mathbb{Q}^p$, where \mathbb{Q} is a learned codebook and p denotes the number of spatial tokens (i.e., divided image patches) in the quantized representation.

There are three common contexts for \mathbf{z} : (1) **Next-token auto-regression**, where tokens are predicted sequentially and the VQ decoder transforms them back into image pixels, as in Emu 3 [45], JanusPro [10], and LlamaGen [42]. (2) **Next-scale autoregression**, where the generator starts

from coarse-scale tokens (e.g., a 1×1 token map) and progressively predicts higher-resolution token maps conditioned on all previous ones, as in VAR [43] and Infinity [18]. (3) **Latent diffusion hybrid**, which combines global latent diffusion for coarse image structure with autoregressive token prediction for sequentially refining discrete latent components, e.g., Kandinsky [2].

3.3. Diffusion.denoiser

In the category of Deiffusion.denoiser, the final step is denoising, applied over three typical input spaces. (1) **Continuous token**: $\mathbb{S}^d := \mathbb{R}^p$. The image is divided into p patches, with tokens represented as continuous embeddings rather than discrete codes. MAR [26] exemplifies this approach, as illustrated in Fig.1(d). (2) **Low-resolution image**: $\mathbb{S}^d := \mathbb{R}^{h_l \times w_l \times 3}$, where $h_l < h, w_l < w$. In this setting, the generator builds images progressively from low to high resolution through multiple upscaling stages, e.g., $64 \times 64 \rightarrow 256 \times 256 \rightarrow 1024 \times 1024$. The final step adds noise to the previous resolution’s image, resizes it to the target size, and applies diffusion denoising. This process is similar to VAE.decoder–latent super-resolution but operates directly in pixel space (see Fig.1(e)). Two training strategies are common: **cascade super-resolution**, where each adjacent low-to-high resolution stage is trained separately (e.g., DALL-E 3 [33] and GLIDE [31]), and **end-to-end super-resolution**, where all stages are trained jointly (e.g., PixelFlow [9]). (3) **Same-size pixels**: $\mathbb{S}^d := \mathbb{R}^{h \times w \times 3}$. The input \mathbf{z} has the same spatial resolution as the target image. It can either represent a low-quality image to be refined by the diffusion denoiser, as in ReflectionFlow [54], or an initial Gaussian noise sample used in conventional diffusion models such as DDPM [19] and DDIM [40] (Fig.1(f)).

3.4. SingleStage.generator

In the setting of SingleStage.generator, $\mathbb{S}^d := \mathcal{N}(\mathbf{0}, \mathbf{I}_d)$. The generator directly maps a sampled noise vector to the final image, as shown in Fig.1(g). This category includes GAN-based approaches such as GigaGAN [20], which produce high-resolution images through large-scale adversarial training, and pixel-wise auto-regressive models like JetFormer [44], which generate images sequentially in an end-to-end fashion.

Algorithm 1 Sample construction from VAE

Input: A real image set $\mathcal{D} = \{\mathbf{x}\}$
Output: The constructed image set $\{\hat{\mathbf{x}}\}$

```
1: Load vae model
2: for each  $\mathbf{x}$  in  $\mathcal{D}$  do
3:    $\mathbf{z} = \text{vae.encode}(\mathbf{x})$ 
4:    $\hat{\mathbf{x}} = \text{vae.decode}(\mathbf{z})$ 
5: end for
6: return  $\{\hat{\mathbf{x}}\}$ 
```

Algorithm 2 Sample construction from VQ

Input: A real image set $\mathcal{D} = \{\mathbf{x}\}$
Output: The constructed image set $\{\hat{\mathbf{x}}\}$

```
1: Load vq model
2: for each  $\mathbf{x}$  in  $\mathcal{D}$  do
3:    $h = \text{vq.encode}(\mathbf{x})$ 
4:    $\mathbf{z} = \text{vq.quantize}(h)$ 
5:    $\hat{\mathbf{x}} = \text{vq.decode}(\mathbf{z})$ 
6: end for
7: return  $\{\hat{\mathbf{x}}\}$ 
```

Algorithm 3 Sample construction from Diffusion

Input: Real images $\mathcal{D} = \{\mathbf{x}\}$
Output: Constructed set $\{\hat{\mathbf{x}}\}$

```
1: Load denoiser model
2: for each  $\mathbf{x}$  in  $\mathcal{D}$  do
3:    $\mathbf{z} = \hat{\mathbf{x}}_T = \alpha\mathbf{x} + \beta\epsilon$ ,
      $\epsilon \sim N(\mathbf{0}, \mathbf{I})$ 
4:   for  $t = T - 1$  to 0 do
5:      $\tilde{\epsilon} = \text{denoiser}(\hat{\mathbf{x}}_{t+1})$ 
6:      $\hat{\mathbf{x}}_t = \text{step}(\hat{\mathbf{x}}_{t+1}, \tilde{\epsilon})$ 
7:   end for
8: end for
9: return  $\{\hat{\mathbf{x}}_0\}$ 
```

Algorithm 4 Sparse sample selection

Input: Constructed image sets: $\mathcal{D}_1 \cup \mathcal{D}_2 \cup \mathcal{D}_3 = \{\hat{\mathbf{x}}\}_{\text{VAE}} \cup \{\hat{\mathbf{x}}\}_{\text{VQ}} \cup \{\hat{\mathbf{x}}\}_{\text{Diffusion}}$, the number of samples to be selected: k
Output: The sparse constructed image set $\{\hat{\mathbf{x}}\}$

```
1: Load pretrained dinov3 model
2: for  $i = 1$  to 3 do
3:   features.append(dinov3( $\hat{\mathbf{x}}$ )) for all  $\hat{\mathbf{x}} \in \mathcal{D}_i$ 
4:   dist = Euclidean_distances(features)
5:    $\mathcal{M}_i = \text{Kmedoids}(\text{dist}, k)$  //a set of  $k$  instances of  $\hat{\mathbf{x}}$ 
6: end for
7: return  $\mathcal{M}_1 \cup \mathcal{M}_2 \cup \mathcal{M}_3$ 
```

4. Method

We aim to investigate whether the final component leaves identifiable traces in generated images when all preceding components are omitted, and how well such traces generalize across different generation architectures. The core idea is to use real images to elicit generation signatures and train a binary classifier on them. Let the training set of real images be denoted as $\mathcal{D} = \{\mathbf{x}\}$, where each image $\mathbf{x} \in \mathbb{R}^{h \times w \times 3}$ is labeled as 1 (indicating a real image). Let $\varphi^*(\cdot) : \mathbb{S}^d \rightarrow \mathbb{R}^{h \times w \times 3}$ represent the optimized final component of a well-trained generative model, where \mathbb{S}^d is an internal space. To simplify notation, we do not distinguish the model’s parameter set from its corresponding mapping function, e.g., φ^* denotes both the mapping function implemented by a network module and its learnable parameters.

The objective function of the proposed AI-generated image detection is the standard cross-entropy on real images and reconstructed counterparts:

$$\mathcal{L}(\theta; \mathcal{E}) := -E_{\mathbf{x} \sim p_{\mathcal{D}}} [\log(\theta(\mathbf{x})) + \log(1 - \theta(\varphi^*(\mathcal{E}(\mathbf{x}))))] \quad (1)$$

where $\mathcal{E}(\cdot) : \mathbb{R}^{h \times w \times 3} \rightarrow \mathbb{S}^d$ maps an RGB image into the latent space. Given a test image \mathbf{x}_t , the classifier trained with Eq. 1 outputs $\theta(\mathbf{x}_t)$, indicating the probability that \mathbf{x}_t is real (1) or AI-generated (0). In this formulation, The en-

coder \mathcal{E} determines the representation from which the corresponding fake image \mathbf{x} is decoded. It is predefined and not co-trained with θ . The following property formulates the intuition behind the choice of \mathcal{E} .

Property 1 (Choice of encoder) *Let \mathcal{E}^* be the encoder jointly optimized with φ^* during generator training, i.e., $(\mathcal{E}^*, \varphi^*) = \arg \min \mathcal{L}_g(\mathcal{E}, \varphi)$, where \mathcal{L}_g is the generation loss. For any encoder \mathcal{E} , under global optimality, $\mathcal{L}(\theta_{\mathcal{E}^*}, \mathcal{E}^*) \leq \mathcal{L}(\theta_{\mathcal{E}}, \mathcal{E})$, where $\theta_{\mathcal{E}} = \arg \min_{\theta} \mathcal{L}(\theta; \mathcal{E})$.*

This property is stated under the idealized assumption of global minimizers. Nevertheless, it suggests that the encoder \mathcal{E}^* , being jointly optimized and distributionally aligned with the decoder φ^* , achieves the minimal attainable expected detection loss among all possible mapping functions \mathcal{E} .

Property 2 (Non-pairwise training) *Let $\mathcal{D} = \{\mathbf{x}\}$ be real samples and $\mathcal{D}' = \{\mathbf{x}' = \varphi(\mathcal{E}(\mathbf{x})) \mid \mathbf{x} \in \mathcal{D}\}$ be constructed samples. Sampling mini-batches independently from \mathcal{D} and \mathcal{D}' , rather than using paired $(\mathbf{x}_i, \mathbf{x}'_i)$, yields a gradient estimator with lower variance by SGD training, i.e., $\text{Var}(\hat{\nabla}_{\theta}^{(I)}) \leq \text{Var}(\hat{\nabla}_{\theta}^{(P)})$, where*

$$\hat{\nabla}_{\theta}^{(I)} = -\frac{1}{B} \sum_{\mathbf{x} \in \mathcal{B}_t} \nabla_{\theta} \log \theta(\mathbf{x}) - \frac{1}{B} \sum_{\mathbf{x}' \in \mathcal{B}'_t} \nabla_{\theta} \log (1 - \theta(\mathbf{x}')),$$

$$\hat{\nabla}_{\theta}^{(P)} = -\frac{1}{B} \sum_{\mathbf{x} \in \mathcal{B}_t} [\nabla_{\theta} \log \theta(\mathbf{x}) + \nabla_{\theta} \log (1 - \theta(\varphi(\mathcal{E}(\mathbf{x})))],$$

and $\mathcal{B}_t \subseteq \mathcal{D}$, $\mathcal{B}'_t \subseteq \mathcal{D}'$ are mini-batches of size B .

A theoretical and empirical justification is provided in Appendix. This property suggests that independently shuffling real and constructed samples reduces the variance of the stochastic gradient, which in turn leads to more stable and faster convergence in SGD [4, 36]. Therefore, it is advantageous to construct the negative sample set \mathcal{D}' offline and sample from \mathcal{D} and \mathcal{D}' independently during SGD training.

Fig. 2 presents an overview of our method. The input is a real image, and the corresponding fake samples are constructed from it using the encoder and decoder. This operation realizes $\varphi \circ \mathcal{E}(\cdot)$ in Eq. 1, leaving detectable traces while preserving the exact semantic content of the real image. The detector θ is implemented using

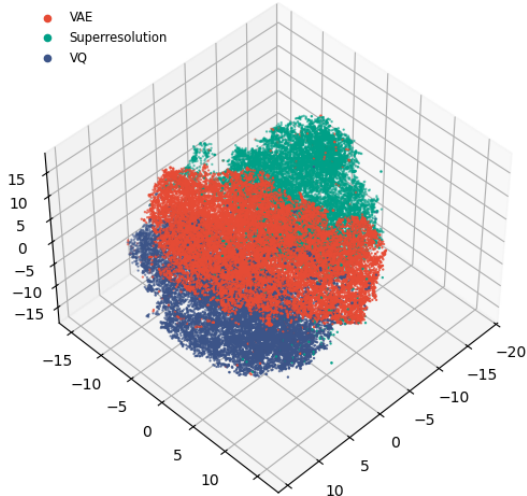


Figure 3. Feature visualization of the three final components.

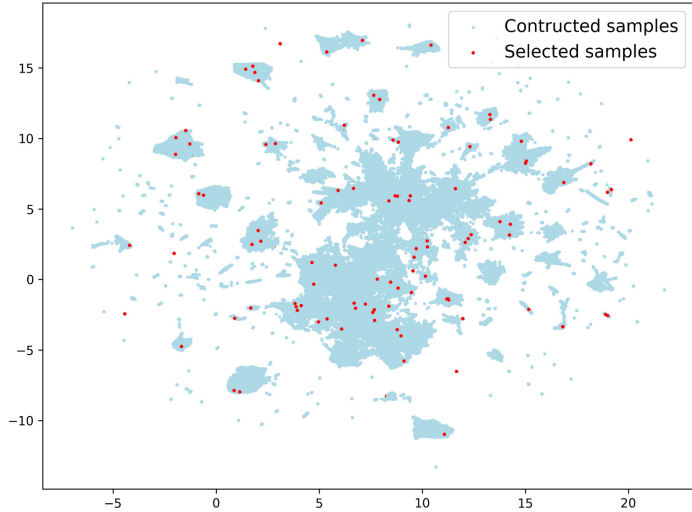


Figure 4. Sparse sample selection.

a pretrained feature extractor (DINOv3) with an additional classification layer. In the following, we detail these two key components of the objective function in Eq. 1: the fake sample construction $\varphi \circ \mathcal{E}(\cdot)$ and the detector θ .

4.1. Fake sample construction — $\varphi \circ \mathcal{E}$

4.1.1. Construction from the three representative components

In our taxonomy (Fig. 1), the three primary categories—VAE.decoder, VQ.de-tokenizer, and Diffusion.denoiser—are defined based on the implementation of the final component, while subcategories are further determined by the input space and functional context in which the component operates. Consequently, all components within the same primary category can share the same algorithmic pipeline for sample construction.

For brevity, we refer to components in these categories as VAE, VQ, and Diffusion respectively in the following sections. As discussed in Property 1, the encoder \mathcal{E}^* , which is pretrained jointly with φ^* , is used to approximate the latent input \mathbf{z} . Algorithm 1 presents the pseudocode for constructing $\varphi^*(\mathcal{E}^*(\mathbf{x}))$ using the VAE. The implementation requires only a few lines of code and is significantly more efficient than executing the full generative pipeline. For VQ, the de-tokenizer acts as φ^* and the image tokenizer as \mathcal{E}^* to approximate image tokens \mathbf{z} , as outlined in Algorithm 2. In Diffusion, the input \mathbf{z} is a noisy version of the input, $\alpha\mathbf{x} + \beta\epsilon_t$, where $\epsilon \sim \mathcal{N}(0, I)$. The noise level can be adjusted by selecting the starting timestep t for denoising (Algorithm 3).

4.1.2. Sparse sampling from combined constructions

As the final components of the three categories differ substantially in both functionality and implementation, the constructed samples $\varphi^*(\mathcal{E}^*(\mathbf{x}))$ from each may exhibit distinct generative traces. We further investigate whether combining a small set of representative fake samples from each component can capture the overall trace space and achieve effective generalization. Algorithm 4 out-

lines the procedure, applying K-Medoids clustering selects k representative samples from the constructed outputs of each component. The selection is performed in a reduced-dimensional feature space. Specifically, the generated samples are first encoded using a pretrained DINOv3 backbone [39], from which 2,048-dimensional feature vectors are extracted from the final layer. K-Medoids selects k samples such that most other samples are close to one of them in Euclidean distance. The selected subsets from all three components are combined to form the final training set of $\varphi^*(\mathcal{E}^*(\mathbf{x}))$ for detector training.

4.2. Detection model θ

Based on the Property 2, instead of loading \mathbf{x} and computing $\varphi^*(\mathcal{E}^*(\mathbf{x}))$ at each training step, we directly input the real image set $\{\mathbf{x}\}$ and the constructed image set $\{\hat{\mathbf{x}}\}$ generated by Algorithms 1–4, with standard shuffling applied to both sets during SGD training. Since the detector θ aims to distinguish subtle differences between real and reconstructed images, and object detection tasks inherently emphasize multi-scale spatial features, we adopt DINOv3—a foundation model pretrained for object detection—as the backbone to better capture fine-grained artifacts. A single fully connected layer is appended to the backbone, and all layers are fine-tuned during training. As our focus is on analyzing the effect of the final generative component, we employ a pretrained visual backbone with minimal modifications rather than designing a complex detector.

5. Experiments

5.1. Model implementation & baselines

Training dataset The real image set used to construct the training dataset in this study is MS-COCO 2014 [28], which contains 118,000 images depicting diverse indoor and outdoor scenes, with resolutions ranging from 384 to 880 pixels in width (or height).

To validate the generalizability of the generator’s final component, we select one representative final component from open-

Table 1. Detection results across different category of generators.

	diffusion.denoiser based						vq.de-tokenizer based				vae.decoder	
	DALL-E 2		DALL-E 3		Glide		Emu3		LlamaGen		HiDream	
	Acc%	AP%	Acc%	AP%	Acc%	AP%	Acc%	AP%	Acc%	AP%	Acc%	AP%
DIRE	56.45	67.05	50.35	53.53	49.50	49.27	53.65	56.73	54.05	59.26	51.40	51.21
LGrad	55.65	55.73	47.65	40.41	47.45	51.83	54.80	48.03	60.70	63.08	40.05	39.06
NPR	49.25	50.18	50.35	50.48	48.80	51.43	51.70	53.05	52.25	55.48	47.75	45.51
FatFormer	54.12	56.02	35.88	33.95	67.77	75.75	63.72	66.10	77.21	87.73	34.48	31.28
RINE	85.90	94.05	42.35	30.83	63.95	72.09	62.10	69.68	90.65	98.36	44.15	39.20
CoDE	54.60	54.26	73.15	72.76	80.75	80.36	77.45	77.06	90.50	90.11	71.45	71.06
C2P-CLIP	55.60	76.87	63.20	90.45	86.65	96.53	68.70	90.60	83.80	97.85	51.20	51.02
AIDE	59.75	42.26	14.15	31.34	59.75	76.71	62.50	56.86	63.25	84.55	48.30	37.95
BFree	93.30	99.16	96.22	99.64	68.61	93.81	99.05	99.97	99.15	99.98	81.40	93.19
Ours_VAE	99.60	100.0	99.70	99.99	98.85	99.92	99.70	99.99	99.70	99.99	99.15	99.94
Ours_VQ	99.80	100.0	99.85	99.99	98.75	99.84	99.85	99.99	99.85	100.0	97.15	99.51
Ours_Diffusion	99.35	99.91	99.85	100.0	98.60	99.85	99.90	100.0	99.90	100.0	88.95	96.95
Ours_Sparse	99.80	99.87	99.15	99.91	98.05	99.47	99.15	99.90	99.15	99.82	96.80	99.21
	vae.decoder based											
	SD1.3		SD1.4		SD XL		SD2		Flux		SD 3.5	
	Acc%	AP%	Acc%	AP%	Acc%	AP%	Acc%	AP%	Acc%	AP%	Acc%	AP%
DIRE	48.75	43.24	48.65	43.38	50.00	58.90	47.45	40.37	61.66	73.10	55.65	58.00
LGrad	54.45	46.46	55.85	48.14	58.65	53.26	48.75	42.80	81.91	91.81	77.29	87.08
NPR	50.70	51.05	50.60	51.69	52.45	55.54	43.50	46.23	90.00	92.34	88.04	89.82
FatFormer	52.97	53.60	53.72	54.07	66.67	75.43	51.57	54.41	55.32	89.83	75.86	95.39
RINE	87.60	95.96	87.15	95.95	74.60	85.56	70.30	80.74	51.70	86.61	96.49	99.93
CoDE	97.75	97.36	97.30	96.91	75.20	74.81	88.05	87.66	71.09	72.17	76.35	75.26
C2P-CLIP	75.15	92.93	76.70	93.03	77.70	94.67	69.15	92.30	53.96	94.58	80.88	98.87
AIDE	57.60	60.25	56.70	60.14	62.70	63.98	53.45	42.09	98.50	99.80	96.45	99.72
BFree	99.25	99.99	99.15	99.99	99.25	99.98	99.80	99.93	69.62	93.62	98.74	99.94
Ours_VAE	99.70	100.0	99.70	100.0	99.70	100.0	99.70	100.0	99.17	99.98	99.96	100.0
Ours_VQ	99.85	100.0	99.85	100.0	99.85	100.0	99.40	99.90	99.19	99.97	99.82	99.99
Ours_Diffusion	99.90	100.0	99.80	100.0	99.90	100.0	99.85	100.0	99.89	100.0	99.86	100.0
Ours_Sparse	99.15	99.90	99.15	99.90	99.15	99.88	99.10	99.80	98.95	98.28	98.98	99.58

source generators for each of the three categories in Fig. 1: *VAE.decoder*, *VQ.detokenizer*, and *Diffusion.denoiser*. Specifically, *Stable Diffusion 2.1* represents the *VAE.decoder* category and is used to construct fake samples following Algorithm 1; *JanusPro* represents the *VQ.detokenizer* category and generates samples according to Algorithm 2; and *PixelFlow* represents the *Diffusion.denoiser* category and follows Algorithm 3. All pretrained encoders \mathcal{E}^* and decoders φ^* are detailed in the Appendix. For brevity, we refer to the corresponding training sets as *VAE*, *VQ*, and *Diffusion* in the following discussion.

These three types of final components exhibit distinct generation traces, as visualized in Fig. 3. Features are extracted from the third layer of a pretrained DINOv3 backbone [39] and projected into three dimensions. Although the resulting distributions exhibit partial overlap, they remain visually separable. To further examine whether a small number of representative samples from each component can capture the overall trace space and achieve effective generalization, we construct an additional compact training set. Specifically, we select 100 samples from each of the *VAE*, *VQ*, *Diffusion* sets using Algorithm 4 with $k = 100$, and refer to it as *Sparse* set in experiments. Fig. 4 visualizes the selection results, where the chosen samples (highlighted in red) are distributed throughout the entire feature space.

Detector implementation To implement the AI-generated image detector, we adopt a pretrained DINOv3 backbone [39] with an additional fully connected layer for binary classification. All layers are fine-tuned using the standard cross-entropy loss in Eq. 1 with a learning rate of 5×10^{-7} . We train separate detectors on the

training sets *VAE*, *VQ*, *Diffusion*, and *Sparse*, and evaluate them on images from different categories in our taxonomy to analyze the effectiveness of the proposed method.

Baselines We compare our method against nine baseline approaches: BFree [17] (CVPR 2025), AIDE [35] (ICLR 2025), C2P-CLIP [51] (AAAI 2025), CoDE [25] (ECCV 2024), RINE [30] (ECCV 2024), FatFormer [29] (CVPR 2024), NPR [24] (CVPR 2024), LGrad [14] (CVPR 2023), and DIRE [22] (ICCV 2023). As these methods either did not report results on all of our test sets or used different evaluation metrics, we re-evaluate each method using its publicly released pretrained model and default hyperparameters. Notably, BFree also evaluated these baselines on a subset of our test sets; our results and conclusions regarding the baseline methods are consistent with those reported in BFree. The source code links, configurations, and pretrained models used are provided in the Appendix. Performance is assessed using two standard metrics: classification accuracy (Acc) and average precision (AP).

5.2. Results across different category of generators

Testing set (1) Synthbuster [3] is a challenging benchmark comprising 1,000 high-resolution real images from RAISE-1K [11] and 1,000 fake images generated by each of nine models: SD1.3, SD1.4, SD2, SDXL, DALL-E2, DALL-E3, Glide, Adobe Firefly and MidJourney v5, using the corresponding 1000 prompts. Based on our proposed taxonomy, these subsets are classified into the *VAE.decoder* and *Diffusion.denoiser* categories, as summarized in Table 1. As the architectures of Firefly and MidJourney are not

Table 2. Detection results on wild generations.

	Unknown architecture		Mixture		Wild generation							
	Firefly		Midjourney		FakeBench		Reddit		Facebook		Twitter	
	Acc%	AP%	Acc%	AP%	Acc%	AP%	Acc%	AP%	Acc%	AP%	Acc%	AP%
DIRE	50.80	55.06	53.90	60.56	44.38	41.72	57.19	61.93	56.56	66.02	47.74	78.72
LGrad	47.25	42.41	57.70	53.09	44.01	69.44	57.80	65.31	66.88	77.26	40.86	61.63
NPR	47.30	46.96	52.35	55.22	52.37	57.85	63.80	66.87	74.06	83.68	48.46	67.53
FatFormer	60.12	62.24	44.43	41.82	71.20	80.93	69.47	80.83	54.83	75.27	42.79	77.41
RINE	92.10	99.71	55.45	59.38	74.77	97.22	71.20	81.28	51.56	55.44	55.93	62.27
CoDE	60.65	60.28	76.90	76.51	74.75	73.94	65.80	61.12	72.19	67.50	68.41	78.34
C2P-CLIP	59.45	82.11	52.85	69.37	74.77	91.18	68.40	78.85	54.37	71.39	47.27	75.07
AIDE	14.40	31.74	53.45	40.43	74.78	86.76	70.87	82.52	50.00	55.96	52.78	59.40
BFree	<u>98.85</u>	<u>99.91</u>	<u>98.70</u>	<u>99.93</u>	<u>80.81</u>	<u>100.0</u>	<u>85.20</u>	<u>94.94</u>	<u>95.31</u>	<u>98.98</u>	<u>95.75</u>	<u>99.42</u>
Ours_VAE	99.70	100.0	99.70	99.99	98.83	99.97	96.87	996.8	97.81	98.99	98.34	99.93
Ours_VQ	99.70	99.99	99.45	99.96	98.10	99.82	95.40	99.80	95.31	99.28	98.34	99.86
Ours_Diffusion	98.50	99.96	99.70	100.0	94.38	99.78	98.67	99.64	97.19	99.46	97.39	99.98
Ours_Sparse	98.00	99.73	99.10	99.90	97.90	99.9	97.60	99.51	98.44	99.44	99.31	100.0

Table 3. Results on finetuned generators.

	Satellite image generation							
	amusement_park		car_dealership		electric_station		stadium	
	Acc%	AP%	Acc%	AP%	Acc%	AP%	Acc%	AP%
DIRE	50.49	85.96	50.19	84.49	50.40	83.85	50.58	94.11
LGrad	48.85	35.98	50.00	42.38	50.15	47.30	50.02	43.46
NPR	46.89	42.62	65.65	92.65	62.52	83.55	56.16	84.64
FatFormer	51.68	69.84	50.88	83.10	52.81	78.68	51.66	83.76
RINE	69.07	82.59	51.97	50.15	64.19	73.99	68.16	78.23
CoDE	86.66	82.00	88.40	83.67	84.50	79.53	78.37	73.16
C2P-CLIP	58.00	75.82	76.60	96.21	71.71	87.63	58.74	93.90
AIDE	52.90	57.74	61.71	84.69	61.11	75.62	52.32	72.37
BFree	<u>95.48</u>	<u>100.0</u>	<u>95.57</u>	<u>99.97</u>	<u>90.75</u>	<u>99.95</u>	<u>88.95</u>	<u>99.98</u>
Ours_VAE	99.33	100.0	96.43	99.96	96.08	99.87	96.50	99.97
Ours_VQ	96.77	100.0	87.52	99.98	90.99	99.89	98.89	99.99
Ours_Diffusion	99.67	99.97	97.94	99.62	96.50	99.17	97.34	99.43
Ours_Sparse	99.61	99.99	98.91	9.994	98.55	99.82	99.59	99.98

disclosed, we treat them as wild generators and evaluate them in Section 5.3.

Since the release of Synthbuster, additional generators have emerged that are not included in the benchmark, including VQ.decoder-based generators and new VAE.decoder-based generators such as HiDream, Flux-dev, and SD3.5. To incorporate these, we generate fake images using two autoregressive VQ.decoder generators, Emu3 and LlamGen, as well as HiDream, all based on the same 1,000 Synthbuster prompts.

(2) Although the AI-generated images in these sub-testing sets come from various generators, the real image set is the same across all subsets. In other words, the model’s classification performance on the real images affects the results for all subsets when computing balanced binary classification accuracy. Moreover, 1,000 images for both the real and fake sets constitute a limited sample size and offer limited diversity. To evaluate more diverse semantic content and larger sample sizes, for Flux-dev and SD3.5, we use 9,600 images from the PASCAL VOC training split [15] as the real image set. For the fake image set, we generate 10,000 images from each generator using short descriptions produced by an LLM. Since the detector identifies generator traces rather than comparing real-AI image pairs, the semantic content differences between PASCAL VOC and the generated images do not affect the evaluation. Instead, the ability of the detector to correctly classify real images containing many small objects, as in PASCAL VOC, is a key aspect of assessing its robustness.

Results Table 1 reports detection results across generator cate-

gories. The best results are highlighted in bold, and the best baseline results are indicated with a wavy underline. It is evident that robustness is a key challenge, especially as new generators continue to emerge. DIRE and LGrad, which were trained on GAN-based data, perform poorly on most modern generators. However, for Flux and SD3.5, LGrad achieves 81.91% accuracy and 91.81% AP. Similarly, RINE, benefiting from CLIP-based features, performs well on some generators, such as LlamaGen (90.65% accuracy) and SD3.5 (96.49%). All baselines published before 2025 struggled to detect DALL-E3 images, a challenge that persisted until BFree was introduced. BFree remains the strongest baseline but still shows limited robustness on Glide, Flux, and HiDream generations. Notably, BFree produces high AP scores even when its prediction accuracy is low. For example, it achieves 69.62% / 96.62% (accuracy / AP) on Flux images, and 68.61% / 93.81% on Glide images. This discrepancy indicates that, although the model ranks positive samples effectively, its thresholded predictions may be incorrect, which may pose challenges in applications that rely on well-calibrated prediction confidence.

In contrast, our approach performs strongly within each category and generalizes effectively across categories, consistently achieving higher accuracy on various subsets. Remarkably, the detector trained on the sparse set, using only 100 fake samples from each of the three components (300 fake and 300 real images in total), achieves performance comparable to our three models trained on individual components with the full MS-COCO dataset. This small training set provides further evidence of the generalization

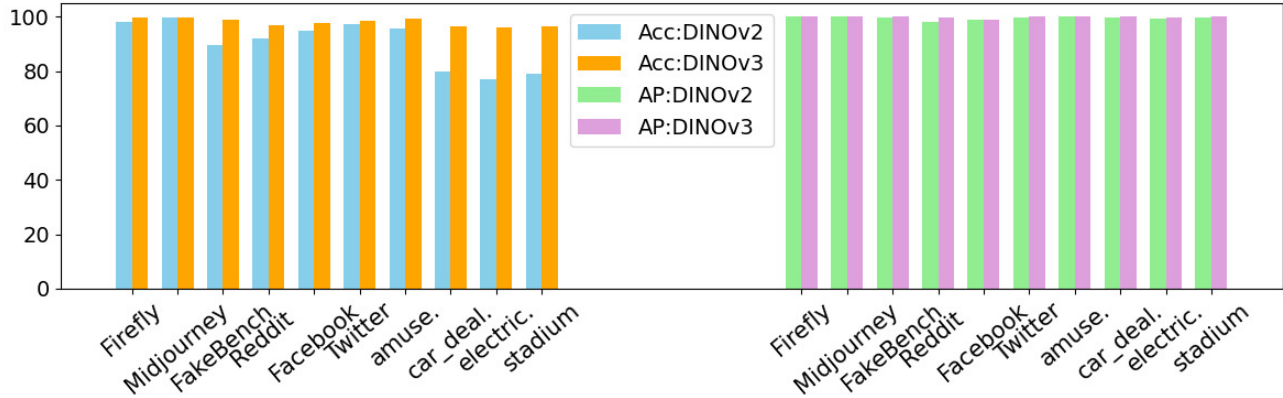


Figure 5. Performances of our detectors with different backbones

capability of our approach and offers a practical advantage, as generating large-scale training images is costly.

5.3. Results on wild generations

Testing set (1) Unknown architectures—Firefly and Midjourney subsets from Synthbuster. Both are commercial generators lacking open-source code or public documentation of their architectures or components. **(2) Mixed generators—FakeBench**[27]. It contains 3,000 real images and 3,000 fake images generated by multiple models. **(3) In-the-wild generation—WildRF**[6]. It comprises three subsets: Reddit, Facebook, and Twitter, each containing real and synthetic images sourced from social media platforms with unknown origins.

Results Table 2 reports the results. Baseline methods exhibit inconsistent results across benchmarks. For instance, RINE performs well on Firefly (92.10% accuracy) but drops sharply on Midjourney (55.45%) and Facebook (51.56%). BFree performs well on most subsets but degrades on FakeBench. This instability underscores the challenge of real-world generalization, particularly in true zero-shot scenarios where no prior information about the generators is available. In contrast, our detector consistently surpasses all baselines and maintains robust, stable performance across all subsets, demonstrating that leveraging traces from the final component yields strong generalization to diverse architectures and challenging real-world conditions.

5.4. Results on domain-specific fine-tuned generators

Testing set SatelliteDiffusion[21] dataset is generated using a satellite imagery model fine-tuned from SD2 and conditioned on satellite metadata. Real images are sourced from high-resolution satellite imagery, while synthetic counterparts are produced using textual descriptions of the real samples. Four subsets: *amusement park*, *car dealership*, *electric substation*, and *stadium* are tested, each including around 2,000 real and 2,000 generated images.

Results Table 3 presents the comparison. Our models achieve results closely matching those reported for the original SD2 evaluations in Table 1, demonstrating that the detection approach remains effective for generators fine-tuned on domain-specific images and

conditions. Baseline models such as CoDE exhibit a similar phenomenon: on SD2, it achieves 88.05% accuracy, while on fine-tuned subsets such as *amusement_park* and *electric_station*, the accuracy slightly decreases to 86.66% and 84.50%, respectively. On the *stadium* subset, both CoDE and the best baseline, BFree, experience larger drops in performance.

5.5. Ablation study

Different backbones To evaluate the impact of the backbone on our detector, we train an additional model using the pretrained DINOv2 backbone. The comparison of performance between DINOv2 and DINOv3 is shown in Fig. 5. The results show that the newer backbone provides a significant improvement in accuracy. For AP, since the margin between the logits of positive and negative images is sufficiently large with DINOv2, using the newer backbone has little effect.

Final component vs. full pipeline To verify whether traces from the final component alone are sufficient to detect images generated by the full pipeline, we train an additional detector on images constructed from the final component of HiDream-I1 on the MS-COCO dataset using Algorithm 1. To evaluate its performance on full-pipeline outputs, we generate test images following Section 5.2 using the 1,000 Synthbuster prompts. The detector achieves 90.5% accuracy and 99% AP, demonstrating that training on the generator’s final component generalizes effectively to its full outputs.

6. Conclusion

This study shows that leveraging the final components of modern image generators offers an effective strategy for improving deepfake detection generalization. By contaminating real images through these components and training on minimal representative samples, the proposed detector achieves superior performance across diverse unseen generators, highlighting the value of insights for robust detection.

References

- [1] Lydia Abady, Jun Wang, Benedetta Tondi, and Mauro Barni. A siamese-based verification system for open-set architec-

- ture attribution of synthetic images. *Pattern Recognition Letters*, 180:75–81, 2024. 2
- [2] Vladimir Arkhipkin, Andrei Filatov, Viacheslav Vasilev, Anastasia Maltseva, Said Azizov, Igor Pavlov, Julia Agafonova, Andrey Kuznetsov, and Denis Dimitrov. Kandinsky 3.0 technical report. [arXiv:2312.03511](https://arxiv.org/abs/2312.03511), 2023. 4
- [3] Quentin Bammey. Synthbuster: Towards detection of diffusion model generated images. *IEEE Open Journal of Signal Processing*, 5:1–9, 2023. 7
- [4] Léon Bottou. Large-scale machine learning with stochastic gradient descent. *19th International Conference on Computational Statistics*, pages 177–187, 2010. 5
- [5] Qi Cai, Jingwen Chen, Yang Chen, Yehao Li, Fuchen Long, Yingwei Pan, Zhaofan Qiu, Yiheng Zhang, Fengbin Gao, Peihan Xu, et al. Hidream-1l: A high-efficient image generative foundation model with sparse diffusion transformer. [arXiv:2505.22705](https://arxiv.org/abs/2505.22705), 2025. 4
- [6] Bar Cavia, Eliahu Horowitz, Tal Reiss, and Yedid Hoshen. Real-time deepfake detection in the real-world. [arXiv:2406.09398](https://arxiv.org/abs/2406.09398), 2024. 9
- [7] Li-Wen Chang, Wenlei Bao, Qi Hou, Chengquan Jiang, Ningxin Zheng, Yinmin Zhong, Xuanrun Zhang, Zuquan Song, Chengji Yao, Ziheng Jiang, et al. Flux: fast software-based communication overlap on gpus through kernel fusion. [arXiv:2406.06858](https://arxiv.org/abs/2406.06858), 2024. 4
- [8] Nora Chen and Oscar Gupta. Lasted: Label-aware synthetic/real text embedding detection. *IEEE/CVF conference on computer vision and pattern recognition (CVPR)*, 2024. 3
- [9] Shoufa Chen, Chongjian Ge, Shilong Zhang, Peize Sun, and Ping Luo. Pixelflow: Pixel-space generative models with flow. [arXiv:2504.07963](https://arxiv.org/abs/2504.07963), 2025. 4
- [10] Xiaokang Chen, Zhiyu Wu, Xingchao Liu, Zizheng Pan, Wen Liu, Zhenda Xie, Xingkai Yu, and Chong Ruan. Januspro: Unified multimodal understanding and generation with data and model scaling. [arXiv:2501.17811](https://arxiv.org/abs/2501.17811), 2025. 4
- [11] Duc-Tien Dang-Nguyen, Cecilia Pasquini, Valentina Conotter, and Giulia Boato. Raise: A raw images dataset for digital image forensics. pages 219–224, 2015. 7
- [12] DeepFloydTeam. Deepfloyd if. <https://github.com/deep-floyd/IF>, 2024. 3, 4
- [13] Jia Deng, Wei Dong, Richard Socher, Li-Jia Li, Kai Li, and Li Fei-Fei. Imagenet: A large-scale hierarchical image database. *IEEE/CVF conference on computer vision and pattern recognition (CVPR)*, pages 248–255, 2009. 2
- [14] Jane Doe and John Smith. Lgrad: Gradient-based fingerprint detection for deepfakes. *IEEE/CVF conference on computer vision and pattern recognition (CVPR)*, 2023. 1, 2, 7
- [15] Mark Everingham, Luc Van Gool, Christopher K. I. Williams, John Winn, and Andrew Zisserman. The PASCAL visual object classes (voc) challenge 2007, 2007. <http://host.robots.ox.ac.uk/pascal/VOC/voc2007/>. 8
- [16] Ian J Goodfellow, Jean Pouget-Abadie, Mehdi Mirza, Bing Xu, David Warde-Farley, Sherjil Ozair, Aaron Courville, and Yoshua Bengio. Generative adversarial nets. *Advances in neural information processing systems (NIPS)*, 27, 2014. 1
- [17] Fabrizio Guillaro, Giada Zingarini, Ben Usman, Avneesh Sud, Davide Cozzolino, and Luisa Verdoliva. A bias-free training paradigm for more general ai-generated image detection. *IEEE/CVF conference on computer vision and pattern recognition (CVPR)*, pages 18685–18694, 2025. 7
- [18] Jian Han, Jinlai Liu, Yi Jiang, Bin Yan, Yuqi Zhang, Zehuan Yuan, Bingyue Peng, and Xiaobing Liu. Infinity: Scaling bit-wise autoregressive modeling for high-resolution image synthesis. [arXiv:2412.04431](https://arxiv.org/abs/2412.04431), 2024. 4
- [19] Jonathan Ho, Ajay Jain, and Pieter Abbeel. Denoising diffusion probabilistic models. *Advances in neural information processing systems (NIPS)*, 33:6840–6851, 2020. 1, 4
- [20] Minguk Kang, Jun-Yan Zhu, Richard Zhang, Jaesik Park, Eli Shechtman, Sylvain Paris, and Taesung Park. Scaling up gans for text-to-image synthesis. *IEEE/CVF conference on computer vision and pattern recognition (CVPR)*, 2023. 4
- [21] Samar Khanna, Patrick Liu, Linqi Zhou, Chenlin Meng, Robin Rombach, Marshall Burke, David B Lobell, and Stefano Ermon. Diffusionsat: A generative foundation model for satellite imagery. *The Twelfth International Conference on Learning Representations (ICLR)*, 2023. 9
- [22] Claire Kim and David Johnson. Dire: Decoder-invertible fingerprint recovery. *IEEE/CVF International Conference on Computer Vision (ICCV)*, 2023. 1, 3, 7
- [23] Mike Laszkiewicz, Jonas Ricker, Johannes Lederer, and Asja Fischer. Single-model attribution of generative models through final-layer inversion. [arXiv:2306.06210](https://arxiv.org/abs/2306.06210), 2023. 2
- [24] Alice Lee and Bob Wang. Npr: Pixel neighborhood difference fingerprints for fake image detection. *IEEE/CVF conference on computer vision and pattern recognition (CVPR)*, 2024. 2, 7
- [25] Ryan Li and Sophie Davis. Code: Contrastive detection engine for multi-scale fake image features. *European Conference on Computer Vision (ECCV)*, 2024. 1, 3, 7
- [26] Tianhong Li, Yonglong Tian, He Li, Mingyang Deng, and Kaiming He. Autoregressive image generation without vector quantization. *Advances in neural information processing systems (NIPS)*, 37:56424–56445, 2024. 3, 4
- [27] Yixuan Li, Xuelin Liu, Xiaoyang Wang, Bu Sung Lee, Shiqi Wang, Anderson Rocha, and Weisi Lin. Fakebench: Probing explainable fake image detection via large multimodal models. *IEEE Transactions on Information Forensics and Security*, 2025. 9
- [28] Tsung-Yi Lin, Michael Maire, Serge Belongie, James Hays, Pietro Perona, Deva Ramanan, Piotr Dollár, and C. Lawrence Zitnick. Microsoft coco: Common objects in context. *European Conference on Computer Vision (ECCV)*, pages 740–755, 2014. 2, 6
- [29] Huan Liu, Zichang Tan, Chuangchuang Tan, Yunchao Wei, Jingdong Wang, and Yao Zhao. Forgery-aware adaptive transformer for generalizable synthetic image detection. *IEEE/CVF conference on computer vision and pattern recognition (CVPR)*, pages 10770–10780, 2024. 7
- [30] George Nguyen and Helen Martinez. Rine: Clip-enhanced deepfake detection via representation integration. [arXiv:2403.54321](https://arxiv.org/abs/2403.54321), 2024. 3, 7

- [31] Alex Nichol and Prafulla Dhariwal. Glide: Towards photo-realistic image generation and editing with text-guided diffusion models. [arXiv:2112.10741](https://arxiv.org/abs/2112.10741), 2021. 4
- [32] Ian Olson and Karen Cho. Defake: Text-guided deepfake detection. [SIGSAC](https://arxiv.org/abs/2303.10000), 2023. 3
- [33] OpenAI. Introducing dall-e 3. <https://openai.com/dall-e-3>, 2023. 4
- [34] OpenAI. Gpt-4o: Openai’s new multimodal model. <https://openai.com/index/gpt-4o>, 2024. 1
- [35] Priya Patel and Quinn Lopez. Aide: Adversarial-inspired detection with frequency domain features. [International Conference on Learning Representations \(ICLR\)](https://arxiv.org/abs/2501.03737), 2025. 1, 3, 7
- [36] Herbert Robbins and Sutton Monro. A stochastic approximation method. [Annals of Mathematical Statistics](https://arxiv.org/abs/1905.08263), 22(3): 400–407, 1951. 5
- [37] Robin Rombach, Andreas Blattmann, Dominik Lorenz, Patrick Esser, and Björn Ommer. High-resolution image synthesis with latent diffusion models. [IEEE/CVF Conference on Computer Vision and Pattern Recognition \(CVPR\)](https://arxiv.org/abs/2205.11485), pages 10684–10695, 2022. 4
- [38] Sowdagar Muhammad Shahid, Sudev Kumar Padhi, Umesh Kashyap, and Sk Subidh Ali. Generalized deepfake attribution. [arXiv:2406.18278](https://arxiv.org/abs/2406.18278), 2024. 2
- [39] Oriane Siméoni, Huy V Vo, Maximilian Seitzer, Federico Baldassarre, Maxime Oquab, Cijo Jose, Vasil Khalidov, Marc Szafraniec, Seungeun Yi, Michaël Ramamonjisoa, et al. Dinov3. [arXiv:2508.10104](https://arxiv.org/abs/2508.10104), 2025. 2, 6, 7
- [40] Jiaming Song, Chenlin Meng, and Stefano Ermon. Denoising diffusion implicit models. [International Conference on Learning Representations \(ICLR\)](https://arxiv.org/abs/2010.02502), 2020. 4
- [41] StabilityAI. Introducing stable diffusion 3.5. <https://stability.ai/news/introducing-stable-diffusion-3-5>, 2024. 4
- [42] Peize Sun, Yi Jiang, Shoufa Chen, Shilong Zhang, Bingyue Peng, Ping Luo, and Zehuan Yuan. Autoregressive model beats diffusion: Llama for scalable image generation. [arXiv:2406.06525](https://arxiv.org/abs/2406.06525), 2024. 4
- [43] Keyu Tian, Yi Jiang, Zehuan Yuan, Bingyue Peng, and Liwei Wang. Visual autoregressive modeling: Scalable image generation via next-scale prediction. [Advances in neural information processing systems \(NIPS\)](https://arxiv.org/abs/2406.18278), 37:84839–84865, 2024. 4
- [44] Michael Tschannen, André Susano Pinto, and Alexander Kolesnikov. Jetformer: An autoregressive generative model of raw images and text. [arXiv:2411.19722](https://arxiv.org/abs/2411.19722), 2024. 4
- [45] Xinlong Wang, Xiaosong Zhang, Zhengxiong Luo, Quan Sun, Yufeng Cui, Jinsheng Wang, Fan Zhang, Yuezhe Wang, Zhen Li, Qiyang Yu, et al. Emu3: Next-token prediction is all you need. [arXiv:2409.18869](https://arxiv.org/abs/2409.18869), 2024. 4
- [46] Zhenting Wang, Vikash Sehwal, Chen Chen, Lingjuan Lyu, Dimitris N Metaxas, and Shiqing Ma. How to trace latent generative model generated images without artificial watermark? [arXiv:2405.13360](https://arxiv.org/abs/2405.13360), 2024. 2
- [47] Yuxiang Wei, Yiheng Zheng, Yabo Zhang, Ming Liu, Zhilong Ji, Lei Zhang, and Wangmeng Zuo. Personalized image generation with deep generative models: A decade survey. [arXiv:2502.13081](https://arxiv.org/abs/2502.13081), 2025. 2
- [48] Alexander Wißmann, Steffen Zeiler, Robert M Nickel, and Dorothea Kolossa. Whodunit: Detection and attribution of synthetic images by leveraging model-specific fingerprints. [3rd ACM International Workshop on Multimedia AI against Disinformation](https://arxiv.org/abs/2406.18278), pages 65–72, 2024. 2
- [49] Katherine Xu, Lingzhi Zhang, and Jianbo Shi. Detecting origin attribution for text-to-image diffusion models in rgb and beyond. [Advances in neural information processing systems \(NIPS\) Safe Generative AI Workshop 2024](https://arxiv.org/abs/2406.18278), 2024. 2
- [50] Tianyun Yang, Ziyao Huang, Juan Cao, Lei Li, and Xirong Li. Deepfake network architecture attribution. [Annual AAAI Conference on Artificial Intelligence \(AAAI\)](https://arxiv.org/abs/2206.04662), 36: 4662–4670, 2022. 2
- [51] Leo Zhang and Maya Kumar. C2p-clip: Contrastive caption prompting for fake image detection. [Annual AAAI Conference on Artificial Intelligence \(AAAI\)](https://arxiv.org/abs/2501.03737), 2025. 1, 3, 7
- [52] Wendi Zheng, Jiayan Teng, Zhuoyi Yang, Weihang Wang, Jidong Chen, Xiaotao Gu, Yuxiao Dong, Ming Ding, and Jie Tang. Cogview3: Finer and faster text-to-image generation via relay diffusion. [European Conference on Computer Vision \(ECCV\)](https://arxiv.org/abs/2406.18278), pages 1–22, 2024. 4
- [53] Emily Zhou and Frank Patel. Univfd: Universal deepfake detection with clip image features. [arXiv:2402.12345](https://arxiv.org/abs/2402.12345), 2024. 3
- [54] Le Zhuo, Liangbing Zhao, Sayak Paul, Yue Liao, Renrui Zhang, Yi Xin, Peng Gao, Mohamed Elhoseiny, and Hongsheng Li. From reflection to perfection: Scaling inference-time optimization for text-to-image diffusion models via reflection tuning. [arXiv:2504.16080](https://arxiv.org/abs/2504.16080), 2025. 4

Exploiting the Final Component of Generator Architectures for AI-Generated Image Detection

Supplementary Material

1. Discussion on Property 2

For convenience, the paired gradient $\hat{\nabla}_\theta^{(P)}$ can be rewritten as:

$$\hat{\nabla}_\theta^{(P)} = -\frac{1}{|\mathcal{B}_t|} \sum_{i=1}^{|\mathcal{B}_t|} \left[\nabla_\theta \log \theta(\mathbf{x}_i) + \nabla_\theta \log(1 - \theta(\varphi(\mathcal{E}(\mathbf{x}_i)))) \right].$$

Define

$$g_i = \nabla_\theta \log \theta(\mathbf{x}_i), \quad g'_i = \nabla_\theta \log(1 - \theta(\varphi(\mathcal{E}(\mathbf{x}_i))),$$

and let

$$G = \{g_i\}_{i=1}^{|\mathcal{B}_t|}, \quad G' = \{g'_i\}_{i=1}^{|\mathcal{B}_t|}.$$

Under this notation, $\hat{\nabla}_\theta^{(P)}$ becomes

$$\hat{\nabla}_\theta^{(P)} = -\frac{1}{|\mathcal{B}_t|} \sum_{i=1}^{|\mathcal{B}_t|} [g_i + g'_i].$$

Since the elements of \mathcal{B}_t are sampled independently, each \mathbf{x}_i is independent of all other samples in \mathcal{B}_t . Consequently, each gradient g_i is independent of all other elements in G except itself, and the same holds for g'_i within G' . Furthermore, g_i is independent of all elements of G' except for its paired counterpart g'_i , and vice versa.

Using the fact that independent random variables have zero covariance, the variance of $\hat{\nabla}_\theta^{(P)}$ is:

$$\begin{aligned} \text{Var}(\hat{\nabla}_\theta^{(P)}) &= \frac{1}{|\mathcal{B}_t|} \sum_{i=1}^{|\mathcal{B}_t|} \left[\text{Var}(g_i) + \text{Var}(g'_i) + 2\text{Cov}(g_i, g'_i) \right] \\ &= \frac{1}{|\mathcal{B}_t|} \left[\text{Var}(G) + \text{Var}(G') + \text{Cov}(G, G') \right], \end{aligned}$$

where

$$\text{Var}(G) = \sum_{i=1}^{|\mathcal{B}_t|} \text{Var}(g_i), \quad \text{Var}(G') = \sum_{i=1}^{|\mathcal{B}_t|} \text{Var}(g'_i),$$

$$\text{Cov}(G, G') = 2 \sum_{i=1}^{|\mathcal{B}_t|} \text{Cov}(g_i, g'_i).$$

In contrast, the variance under independent sampling is

$$\text{Var}(\hat{\nabla}_\theta^{(I)}) = \frac{1}{|\mathcal{B}_t|} \text{Var}(G) + \frac{1}{|\mathcal{B}_t|} \text{Var}(G').$$

The only difference between the two variances is the covariance term $\text{Cov}(G, G')$, which aggregates the individual covariances between g_i and g'_i . Our key observation is that \mathbf{x}_i and its transformed version $\mathbf{x}'_i = \varphi(\mathcal{E}(\mathbf{x}_i))$ are highly similar, and thus their gradients g_i and g'_i tend to be positively correlated. Therefore, $\text{Cov}(g_i, g'_i) > 0$, implying $\text{Cov}(G, G') > 0$. As a result,

$$\text{Var}(\hat{\nabla}_\theta^{(P)}) > \text{Var}(\hat{\nabla}_\theta^{(I)}).$$

This confirms our claim that the gradient estimator achieves lower variance when mini-batches are sampled independently from \mathcal{D} and \mathcal{D}' .

We empirically compare pairwise training with independent training. Using the training set VAE, we train detectors with identical model architectures, hyperparameters, and training data. The only difference lies in how mini-batches are constructed: pairwise training loads matched pairs $(\mathbf{x}, \mathbf{x}')$ into the same mini-batch, whereas independent training samples \mathbf{x} and \mathbf{x}' independently and loads them separately, while ensuring that each mini-batch contains the same number of positive samples \mathbf{x} and negative samples \mathbf{x}' . Table A reports the results. We copy the baseline numbers and *Ours_vae* results from Table 1 of the main paper, along with the additional row for pairwise training. The average accuracy of pairwise training is 97.22%, compared to 99.22% for independent training—a 2% gap. This empirical observation suggests that pairwise training does not provide an advantage over independent training, consistent with our theoretical analysis above.

2. Evidence sources for categorization

Table B summarizes the sources used to determine the final-component category of each generator. For all open-source models, we list the exact commit version, together with the file paths and line numbers that invoke the final component. DALL-E 2 provides only documentation rather than code, and DALL-E 3 has neither detailed documentation nor public source code. Among the listed generators, Flux-1-dev has two widely used official implementations: the Diffusers version operates in latent space and uses a VAE decoder as its final component, while the Black Forest Labs implementation performs generation directly in pixel space. A similar situation appears in DeepFloyd IF: its Stage III super-resolution step has two variants—one based on the Stable Diffusion $\times 4$ latent upsampler, and another implemented in pixel space. Moreover, although MAR is grouped under the “denoiser” category, its final step is a decoder network structurally similar to a U-Net denoiser but without any noise addition or removal.

3. Baseline models

As none of the baseline methods report results on our testing sets, we re-evaluate all of them using their publicly released pretrained models and default hyperparameters. All baselines compute Accuracy and AP using the same functions from `sklearn.metrics: accuracy_score` and `average_precision_score`. The only exception is CoDE, which does not include AP computation in its evaluation code; for this case, we add the same AP calculation used by the other baselines. Below, we provide the links to the testing code and pretrained weights. For each baseline, we use the default hyperparameters specified in the authors’ example scripts within their repositories.

- **DIRE** (ICCV 2023): Testing code from <https://github.c>

Table A. Comparison between pairwise training and independent training.

	diffusion.denoiser based						vq.de-tokenizer based				vae.decoder	
	DALL-E 2		DALL-E 3		Glide		Emu3		LlamaGen		HiDream	
	Acc%	AP%	Acc%	AP%	Acc%	AP%	Acc%	AP%	Acc%	AP%	Acc%	AP%
DIRE	56.45	67.05	50.35	53.53	49.50	49.27	53.65	56.73	54.05	59.26	51.40	51.21
LGrad	55.65	55.73	47.65	40.41	47.45	51.83	54.80	48.03	60.70	63.08	40.05	39.06
NPR	49.25	50.18	50.35	50.48	48.80	51.43	51.70	53.05	52.25	55.48	47.75	45.51
FatFormer	54.12	56.02	35.88	33.95	67.77	75.75	63.72	66.10	77.21	87.73	34.48	31.28
RINE	85.90	94.05	42.35	30.83	63.95	72.09	62.10	69.68	90.65	98.36	44.15	39.20
CoDE	54.60	54.26	73.15	72.76	80.75	80.36	77.45	77.06	90.50	90.11	71.45	71.06
C2P-CLIP	55.60	76.87	63.20	90.45	86.65	96.53	68.70	90.60	83.80	97.85	51.20	51.02
AIDE	59.75	42.26	14.15	31.34	59.75	76.71	62.50	56.86	63.25	84.55	48.30	37.95
BFree	93.30	99.16	96.22	99.64	68.61	93.81	99.05	99.97	99.15	99.98	81.40	93.19
Ours_VAE	99.60	100.0	99.70	99.99	98.85	99.92	99.70	99.99	99.70	99.99	99.15	99.94
Ours_VAE_pair	98.10	99.98	98.20	99.70	98.05	99.91	98.20	99.98	98.20	99.98	97.55	99.27
	vae.decoder based											
	SD1.3		SD1.4		SD XL		SD2		Flux		SD 3.5	
	Acc%	AP%	Acc%	AP%	Acc%	AP%	Acc%	AP%	Acc%	AP%	Acc%	AP%
DIRE	48.75	43.24	48.65	43.38	50.00	58.90	47.45	40.37	61.66	73.10	55.65	58.00
LGrad	54.45	46.46	55.85	48.14	58.65	53.26	48.75	42.80	81.91	91.81	77.29	87.08
NPR	50.70	51.05	50.60	51.69	52.45	55.54	43.50	46.23	90.00	92.34	88.04	89.82
FatFormer	52.97	53.60	53.72	54.07	66.67	75.43	51.57	54.41	55.32	89.83	75.86	95.39
RINE	87.60	95.96	87.15	95.95	74.60	85.56	70.30	80.74	51.70	86.61	96.49	99.93
CoDE	97.75	97.36	97.30	96.91	75.20	74.81	88.05	87.66	71.09	72.17	76.35	75.26
C2P-CLIP	75.15	92.93	76.70	93.03	77.70	94.67	69.15	92.30	53.96	94.58	80.88	98.87
AIDE	57.60	60.25	56.70	60.14	62.70	63.98	53.45	42.09	98.50	99.80	96.45	99.72
BFree	99.25	99.99	99.15	99.99	99.25	99.98	99.80	99.93	69.62	93.62	98.74	99.94
Ours_VAE	99.70	100.0	99.70	100.0	99.70	100.0	99.70	100.0	99.17	99.98	99.96	100.0
Ours_VAE_pair	98.20	99.99	98.20	99.99	98.20	99.92	98.20	99.93	98.88	95.42	99.07	97.75

om/ZhendongWang6/DIRE. We use the pretrained model `lsun_adm.pth` downloaded from the provided checkpoints.

- **LGrad** (CVPR 2023): Testing code from <https://github.com/chuangchuangtan/LGrad>, with pretrained weights `LGrad-4class-Trainon-Progan_car_cat_chair_horse.pth`.
- **NPR** (CVPR 2024): Testing code from <https://github.com/chuangchuangtan/NPR-DeepfakeDetection>, with pretrained weights `model_epoch_last_3090.pth`.
- **FatFormer** (CVPR 2024): Testing code from <https://github.com/Michel-liu/FatFormer>, using `fat-former_4class_ckpt.pth`.
- **RINE** (ECCV 2024): Testing code from <https://github.com/mever-team/rine>, using `model_ldm_trainable.pth`.
- **CoDE** (ECCV 2024): Testing code from <https://github.com/aimagelab/CoDE>, with the pretrained classifier available at https://huggingface.co/aimagelab/CoDE/tree/main/sklearn/linear_tot_classifier_epoch-32.sav.
- **C2P-CLIP** (AAAI 2025): Testing code from <https://github.com/chuangchuangtan/C2P-CLIP-DeepfakeDetection>, using the released weights at https://www.now61.com/f/950efw/C2P_CLIP_release_20240901.zip/C2P_CLIP_release_20240901.pth.
- **AIDE** (ICLR 2025): Testing code from <https://github.com/shilinyan99/AIDE>, using `progan_train.pth`.
- **BFree** (CVPR2025): Testing code from <https://github.com/grip-unina/B-Free>, using weights https://www.grip.unina.it/download/prog/B-Free/weights/BFREE_dino2reg4.zip.

4. Datasets construction

Based on **Property 2**, we generate the constructed image sets \mathcal{x}' offline and save them before training begins. For each of the three representative final components—*Stable Diffusion 2.1*, *JanusPro* and *PixelFlow*, the corresponding constructed training set is produced using its well-trained, optimized encoder, following the guidance of **Property 1**. Below, we list the real images and the pretrained \mathcal{E}^* and φ^* used in our experiments:

- **VAE training set** (Sec 5.1): The real images are from the full MS-COCO 2014 dataset (118k images). The pretrained VAE used to generate negative samples is the VAE from <https://huggingface.co/stabilityai/stable-diffusion-2-1>.
- **VQ training set** (Sec 5.1): The pretrained model used for converting real images is *JanusPro-7B* <https://huggingface.co/deepseek-ai/Janus-Pro-7B>. Due to its fixed patch size, Janus only supports a resolution of 378×378. Therefore, we filter out images smaller than this size and center-crop the remaining MS-COCO images to 378×378.
- **Diffusion training set** (Sec 5.1): We use *PixelFlow* <https://huggingface.co/ShoufaChen/PixelFlow-Text2Image/tree/main/model.pt>, whose last stage is pretrained to upscale images from 128×128 to 512×512. For real images in MS-COCO, we crop them to 512×512 whenever the resolution allows. We do not downsample and re-upsample the real images; instead, we directly use real images that match the output resolution.
- **HiDream training set** (Sec 5.5): The pretrained VAE weights are from *HiDream-I1-Full* <https://huggingface.co/HiDream-ai/HiDream-I1-Full>.

For the testing set, we use the full sets from the benchmarks

Table B. Sources for generator categorization.

Name	Category	Source	Evidence	
Stable Diffusion 3.5	vae.decoder	https://github.com/Stability-AI/sd3.5	Commit 106db06 sd3.infer.py : Line 495	image = self.vae_decode(sampled_latent)
Flux 1-dev	vae.decoder	https://github.com/huggingface/diffusers/tree/main/src/diffusers/pipelines/flux	Commit 5e181ed pipeline_flux.py : Line 1006	image = self.vae.decode(latents, return_dict=False)[0]
	diffusion.denoiser	https://github.com/black-forest-labs/flux	Commit 57ce405 src/flux/sampling.py : Line 351	img = img + (t.prev - t.curr) * pred
HiDream-II	vae.decoder	https://github.com/HiDream-ai/HiDream-II	Commit 3519729 hi_diffusers/pipelines/hidream_image/pipeline_hidream_image.py : Line 724	image = self.vae.decode(latents, return_dict=False)[0]
Stable diffusion xl	vae.decoder	https://github.com/huggingface/diffusers/tree/main/src/diffusers/pipelines/stable_diffusion_xl	Commit 0d1c5b0 pipeline_stable_diffusion_xl.py : Line 1292	image = self.vae.decode(latents, return_dict=False)[0]
CogView4	vae.decoder	https://github.com/huggingface/diffusers/blob/main/src/diffusers/pipelines/cogview4	Commit 0d1c5b0 pipeline_cogview4.py : Line 673	image = self.vae.decode(latents, return_dict=False, generator=generator)[0]
DeepFloyd IF	vae.decoder	https://github.com/deep-floyd/IF/	Commit af64403 deepfloyd_if/modules/stage_III_sd_x4.py : Line 80	available_models = ['stable-diffusion-x4-upscaler'] ... images = self.model(**metadata).images
	diffusion.denoiser	https://github.com/deep-floyd/IF/	Commit a4df8db pipeline_stable_diffusion_upscale.py : Line 798 Commit af64403 deepfloyd_if/modules/stage_III.py:Line 26 Commit af64403 deepfloyd_if/modules/base.py : Line 194	image = self.vae.decode(latents / self.vae.config.scaling_factor, return_dict=False)[0] return super().embeddings_to_image(...) sample = diffusion.p_sample_loop(...)
Kandinsky 3.0	vq.de-tokenizer	https://github.com/ai-forever/Kandinsky-3	Commit 10db67a kandinsky3/movq.py: Line 420,421	decoder_input = self.post_quant_conv(quant) decoded = self.decoder(decoder_input, quant)
Emu3	vq.de-tokenizer	https://github.com/baaivision/Emu3	Commit 1a43ee6 emu3/mlm/processing_emu3.py : Line 198, 199	doc=self.tokenizer.decode(*args,**kwargs) return self.multimodal_decode(doc)
JanusPro	vq.de-tokenizer	https://github.com/deepseek-ai/Janus	Commit 659982f janus/models/vq_model.py: Line 506,507	quant_b = self.quantize.get_codebook_entry() dec = self.decode(quant_b)
LlamaGen	vq.de-tokenizer	https://github.com/FoundationVision/LlamaGen	Commit 5a50452 autoregressive/sample/sample_t2i.py : Line 121	samples = vq_model.decode_code(index_sample, qzshape)
Infinity	vq.de-tokenizer	https://github.com/FoundationVision/Infinity	Commit 3ab8e0c infinity/models/infinity.py : Line 636	img = vae.decode(summed_codes.squeeze(-3))
VAR	vq.de-tokenizer	https://github.com/FoundationVision/VAR	Commit a5cf0a1 models/var.py : Line 190	return self.vae_proxy[0].f_hat_to_img(f_hat) // self.vae_proxy: Tuple[VQVAE]
MAR	decoder	https://github.com/LTH14/mar	Commit fe1de72 models/mar.py : Line: 225	x = block(x)
DALL-E 2	diffusion.denoiser	Document: Hierarchical Text-Conditional Image Generation with CLIP Latents	Page 4	"we train two diffusion upsampler models: one to upsample images from 64x64 to 256x256 resolution, and another to further upsample those to 1024x1024 resolution"
GLIDE	diffusion.denoiser	https://github.com/openai/glide-text2im	Commit 1f791b8 glide.text2im/text2im_model.py: Line 167	return super().forward(x, timesteps, **kwargs)
PixelFlow	diffusion.denoiser	https://github.com/ShoufaChen/PixelFlow	Commit eeabc08 pixelflow/pipeline_pixelflow.py : Line 253	latents = self.scheduler.step(model_output=noise_pred, sample=latents)
Reflection-Flow	diffusion.denoiser	https://github.com/Diffusion-CoT/ReflectionFlow	train_flux/sample.py : inference-time refine by black-forest-labs/FLUX.1-dev	Flux-1-dev (pixel-space implementation; see note above)
DDPM	diffusion.denoiser	https://github.com/hojonathano/diffusion	Commit c461299 diffusion_tf/diffusion_utils_2.py : Line 211	self.p_sample(..., x=img_, ...)
DDIM	diffusion.denoiser	https://github.com/huggingface/diffusers/tree/main/src/diffusers/pipelines/ddim	Commit a4df8db pipeline_ddim.py : Line 152	image = self.scheduler.step(...)
GigaGAN	one-stop.generator	https://github.com/lucidrains/gigagan-pytorch	Commit 0806433 gigagan_pytorch/gigagan_pytorch.py: Line 2167, 2169	model = self.G_ema if self.has_ema_generator else self.G return model(*args, **kwargs)
JetFormer	one-stop.generator	https://github.com/google-research/big_vision	Commit 9c006bf big_vision/models/proj_jetformer/jetformer.py: Line 481	pre_logits, decoder_out = self.decoder(x, ...)

Synthbuster, FakeBench, and WildRF. In Synthbuster, there are 1,000 high-resolution real images from RAISE-1K, along with 1,000 fake images generated by each of nine models: DALL-E2, DALL-E3, Adobe Firefly, MidJourney v5, SD1.3, SD1.4, SD2, SDXL, and Glide. The corresponding columns in Tables 1 and 2 correspond to these subsets. To include more recent generators, we additionally construct the following test sets used in the experiments reported in the main paper:

- **HiDream, Emu3, and LlamaGen** (Table 1): Real images are the same as in Synthbuster. Fake images are generated from the same 1,000 prompts used for the original nine generators (listed in `prompts.csv` in <https://zenodo.org/records/10066460/files/synthbuster.zip>). Generation parameters and image resolutions follow the defaults in each repository, as listed in Table B.
- **Flux-1-dev and SD3.5** (Table 1): We generate additional large-scale test sets from SD3.5 (<https://github.com/Stability-AI/sd3.5>) and Flux-1-dev (<https://github.com/huggingface/diffusers/tree/main/src/diffusers/pipelines/flux>), with 10,000 fake images each.
- **SatelliteDiffusion testing set** (Table 3): The real images comprise all images from four categories of the fMoW validation set (<https://github.com/fMoW/dataset>): amusement park (2,556 images), car dealership (2,156 images), electric substation (2,626 images), and stadium (2,575 images). Each real image has associated metadata including location (country). Fake images are generated from <https://github.com/amar-khanna/DiffusionSat> using prompts of the form: “a fMoW satellite image of {class_name} in {country}”. The number of generated images matches the number of real images for each class.